metals

MDPI

Article

Optimization of Process Parameters and Microstructure of CoCrFeNiTiAl High-Performance High-Entropy Alloy Coating

Bingchun Jiang [1,*], Zhu Huang [1,2], Cunyu Liu [2], Huipeng Wang [2], Fengyuan Shu [3], Yuncai Zhao [1] and Heping Lei [1,4]

[1] School of Mechanical and Electrical Engineering, Guangdong University of Science and Technology, Dongguan 523083, China; 17370461803@163.com (Z.H.); zhaoyuncai@gdust.edu.cn (Y.Z.); peacelei@163.com (H.L.)
[2] School of Mechanical and Electrical Engineering, Jiangxi University of Science and Technology, Ganzhou 341000, China; lcy19954623@163.com (C.L.); wanghuipeng1983@126.com (H.W.)
[3] School of Chemical Engineering and Technology, Sun Yat-sen University, Zhuhai 519082, China; shufy6@mail.sysu.edu.cn
[4] School of Materials Science and Engineering, Hunan University of Science and Technology, Xiangtan 411201, China
* Correspondence: jiangbingchun_2008@163.com; Tel.: +86-15728134593

Abstract: CoCrFeNiTiAl high-entropy alloy coatings have been prepared by laser cladding technology based on response surface methodology (RSM). The results show that the effects of laser power, cladding speed, and pulse width on the dilution rate and microhardness of the high-entropy alloy coatings are investigated. Among the single-factor results, the laser power has the most significant effect on the properties of high-entropy alloy coatings, followed by the cladding speed, while the pulse width has no significant effect. In the interaction term analysis, the interaction term of laser power and pulse width has a remarkable effect on both output responses, whereas the interaction term of pulse width and cladding speed only has a considerable effect on microhardness, while the interaction term of laser power and cladding speed has an insignificant effect on both output responses. The optimum parameters for the preparation of high-performance high-entropy alloy coatings are found at laser power P = 676.73 W, cladding speed V = 5 mm/s, and pulse width P_0 = 9 ms. The microstructures of the high-entropy alloy coating prepared with optimal process parameters have been characterized, which show that the metallurgical bonding between the cladding layer and the substrate is strong and without obvious defects such as porosity and cracks.

Keywords: high-entropy alloy; response surface methodology; process parameters; laser cladding

check for updates

Citation: Jiang, B.; Huang, Z.; Liu, C.; Wang, H.; Shu, F.; Zhao, Y.; Lei, H. Optimization of Process Parameters and Microstructure of CoCrFeNiTiAl High-Performance High-Entropy Alloy Coating. *Metals* **2024**, *14*, 1384. https://doi.org/10.3390/met14121384

Academic Editor: Cristian Ciobanu

Received: 30 October 2024
Revised: 27 November 2024
Accepted: 30 November 2024
Published: 2 December 2024

Copyright: © 2024 by the authors. Licensee MDPI, Basel, Switzerland. This article is an open access article distributed under the terms and conditions of the Creative Commons Attribution (CC BY) license (https://creativecommons.org/licenses/by/4.0/).

1. Introduction

High-entropy alloys are defined as solid solution alloys consisting of five or more major metallic elements with the atomic percentages of each element ranging from 5% to 35% [1–3]. As a new type of metallic material, high-entropy alloys have excellent specific strength, high corrosion resistance, high yield stress, and excellent fracture resistance [4,5]. In the HEA system, CoCrCuFeNi with a face-centered cubic structure and CoCrFeNiAl with a body-centered cubic structure have been studied the most. Due to the fact that the CoCrFeNiAl system is a simple and fundamental system, it is often used to analyze the relationship between the microstructure and properties of HEAs [6], which are used in many high-end industrial fields with their unconventional design concepts and unique performance advantages [7]. Currently, there are many methods to prepare high-entropy alloy coatings, such as laser cladding, thermal spraying, magnetron sputtering, and arc melting [8,9]. Compared with other surface strengthening techniques, laser cladding can form a good metallurgical bond between the coating and the substrate, and the dilution rate and heat-affected zone are small, so that fine microstructures can be formed [10]. Since

unreasonable process parameter settings can lead to the degradation of coating properties, the selection of appropriate process parameters is crucial for the final high-entropy alloy coating performance [11]. Process parameter optimization based on single-layer coatings has great application value, and the response surface methodology can be used to obtain the best combination of different process parameters with fewer experiments, which is the most important method for optimizing the process parameters of laser cladding [12].

Xu et al. [13] prepared $CoCrCu_{0.4}FeNi$ high-entropy alloy coating by laser cladding. It was found that the lower the laser power and the faster the scanning speed, the lower the dilution rate of the steel substrate, and therefore the stronger the fine grain strengthening effect of the coating, resulting in a higher hardness of the coating. Moreover, Shu et al. [14] found that an increase in laser power leads to a decrease in the content of amorphous phases within the coating, which results in a decrease in microhardness and wear resistance. Cao et al. [15] investigated the effect of laser cladding process parameters on the properties of the cladding layers for the preparation of NiCrCoAlY high-entropy alloys. The results show that the laser power is positively correlated with the height, width, and dilution rate of the cladding layer. In addition, the scanning speed was negatively correlated with the height and width of the cladding layer, and positively correlated with the dilution rate.

The above results indicate that process parameters can have a significant impact on the properties of high-entropy alloy coatings. Previously, there are few reports on the effect of various process parameters on the dilution rate and microhardness. In order to explore the effects of laser power, cladding speed, and pulse width on the dilution rate and microhardness, CoCrFeNiTiAl high-entropy alloy coating on H13 die steel substrate was investigated based on response surface methodology (RSM), and the data obtained after the test were analyzed and optimized by design of experiments (DOEs) to reduce the experimental workload and realize the optimal value of each parameter. Finally, the high-entropy alloy coatings were prepared using the optimized process parameters and their microstructures were characterized. Overall, this study is expected to provide important theoretical support and practical application value for the preparation of high-performance high-entropy alloy coatings.

2. Experimental Design of Response Surface Method

2.1. Response Surface Methodology

Response surface methodology is a design of experiments technique that mathematically fits the experimental field studied in a theoretical design using a response function. In this study, laser power (P), cladding speed (V), and pulse width (P_0) were used as input variables, and the dilution rate (η) and microhardness (H) were employed as output responses, respectively. The three-factor second-order response surface model is represented by Equation (1), while the expression for the dilution rate is defined by Equation (2).

$$Y = \beta_0 + \sum_{i=1}^{k} \beta_i X_i + \sum_{i=1}^{k} \beta_{ii} X_i^2 + \sum_{i}^{k} \sum_{j}^{k} \beta_{ij} X_i X_J + \varepsilon \quad (1)$$

$$\text{Dilution rate} = \frac{h}{H + h} \times 100\% \quad (2)$$

where X represents the input variable and Y is the output response. β_0 indicates the coefficient of the constant term. β_i, β_{ii}, and β_{ij} denote the coefficients of linear effect, secondary effect, and interaction effect, respectively. X_i, $X_i{}^2$, and X_iX_j refer to the significant terms of independent variables in the regression model, respectively. ε stands for the experimental error. Finally, ANOVA analysis was performed to evaluate the effectiveness of the model.

2.2. ANOVA Analysis

ANOVA analysis is a type of regression analysis that examines the effect of each input variable on the output response by identifying the significant factors influencing the process

based on the preferred confidence intervals in the model. The F-number is used to verify whether the model is significant or not, and the mean square of the residuals is compared to the mean square. If the F-value is close to 1, the input variable is unlikely to have a significant effect on the output response. The effect of the input variable on the output response is proportional to the F-value, and the higher the F-value, the more significant the effect of the variable on the output response. Notably, the level of significance of each factor on the different output responses was calculated by the *t*-test and *p*-value along with 95% confidence interval. If the *p*-value is greater than 0.05, the input variable has no notable effect on the output response. Variance (R^2) is the coefficient that determines the applicability of the model. One-way plots, interaction plots, and perturbation plots were used to explain the relationship between the output response and the independent variables. This study used Design Expert 13 software to conduct Box Behnken design (BBD) on experimental samples through DOE, and performed ANOVA analysis on the data obtained after the experiment.

2.3. Design of Experiments

Design of experiments (DOEs) is a statistical tool used to design, develop, and optimize many types of systems, processes, and products [16]. The range of process parameters shown in Table 1 was determined on the premise that the coating could be continuous and free from significant surface defects. In the experimental design, a three-factor, three-level surface analysis was performed with each process parameter divided into three levels, namely −1 (lower), 0 (center point), and 1 (higher). The output responses were the dilution rate (η) and microhardness (H). Figure 1 shows a schematic cross-section of a typical laser cladding coating.

Table 1. Input factors with design level.

Factors	Units	Levels		
		−1	**0**	**1**
Laser power	W	600	800	1000
Cladding speed	mm/s	2	3.5	5
Pulse width	ms	7	8	9

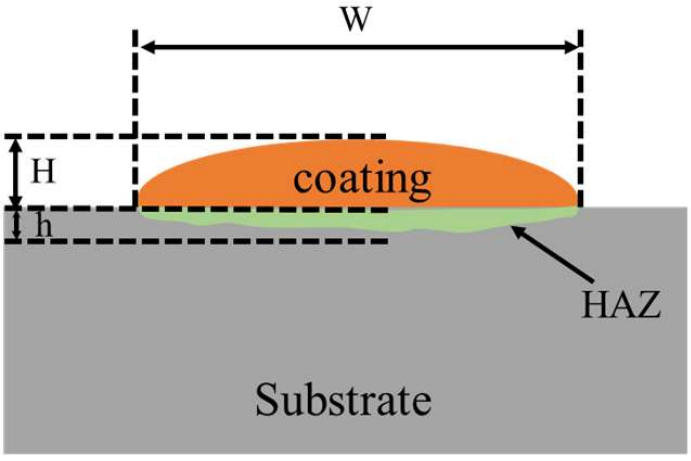


Figure 1. Schematic cross-section of laser cladding.

Table 2 shows the BBD matrix obtained from the experimental design and the corresponding output responses. A total of 17 sets of experiments were conducted through the BBD design.

Table 2. BBD matrix and output responses.

Standard Sequence	Running Sequence	Input Variables			Output Response	
		Laser Power (W)	Cladding Speed (mm/s)	Pulse Width (ms)	Hardness (HV)	Dilution Rate (%)
13	1	800	3.5	8	723.02 ± 0.03	14.53 ± 0.02
2	2	1000	2	8	704.62 ± 0.01	24.60 ± 0.02
17	3	800	3.5	8	713.54 ± 0.01	14.57 ± 0.01
16	4	800	3.5	8	713.62 ± 0.02	15.06 ± 0.03
8	5	1000	3.5	9	715.71 ± 0.04	20.58 ± 0.05
9	6	800	2	7	729.72 ± 0.03	16.84 ± 0.01
10	7	800	5	7	715.56 ± 0.04	12.58 ± 0.01
6	8	1000	3.5	7	700.13 ± 0.01	22.57 ± 0.02
11	9	800	2	9	722.44 ± 0.06	17.53 ± 0.03
5	10	600	3.5	7	719.82 ± 0.02	10.06 ± 0.03
14	11	800	3.5	8	716.52 ± 0.04	15.03 ± 0.01
3	12	600	5	8	711.56 ± 0.03	9.56 ± 0.02
12	13	800	5	9	724.65 ± 0.02	13.68 ± 0.01
15	14	800	3.5	8	717.64 ± 0.01	14.68 ± 0.02
7	15	600	3.5	9	713.73 ± 0.03	11.30 ± 0.01
4	16	1000	5	8	703.62 ± 0.03	19.56 ± 0.06
1	17	600	2	8	724.47 ± 0.06	13.52 ± 0.03

3. Materials and Methods

The substrate material selected for the test was H13 mold steel, with a size of 100 mm × 50 mm × 5 mm and a hardness of 470 HV. The laser cladding material is CoCrFeNiTiAl high-entropy alloy powder prepared by the aerosol method, with a purity of 99.99% and an average particle size of 50 μm. Mix the powder uniformly by ball milling at a speed of 300 rpm and a ball to powder ratio of 2:1 (mass ratio) for two hours. Figure 2 shows the microstructure of the alloy powder after ball milling and mixing.

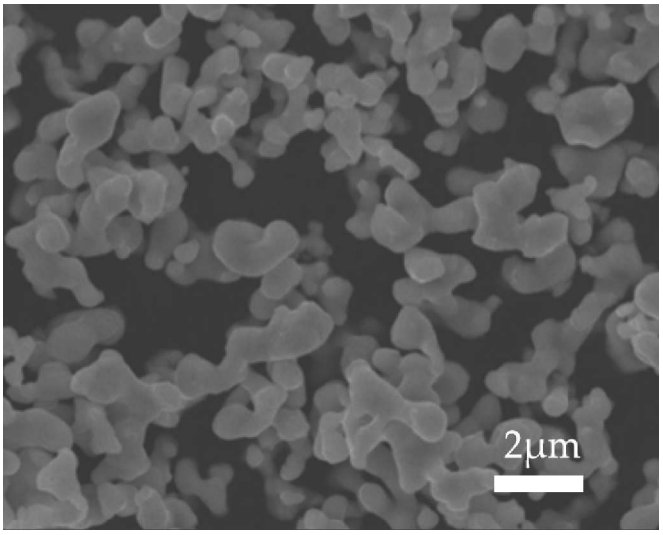


Figure 2. Shows the SEM image of the microstructure of the alloy powder after ball milling and mixing.

Before the test, 400 #~1200 # silicon carbide sandpaper was used to polish gradually to remove the oxidized film on the surface of the H13 matrix. After the surface was bright, it was rinsed in ethanol with an ultrasonic cleaner for 10 min, and finally removed and dried in a dryer at 240 °C. Prior to laser cladding, mix the powder to be melted evenly with adhesive to form a paste, and place it in a syringe type extrusion mold to pre-coat the powder on the surface of the substrate by extrusion. Let it dry to form a pre-coating layer. It was then placed in a studio and argon gas with a purity of 99.999% was introduced as a shielding gas, and finally the cladding parameters were adjusted and optimized. Laser cladding was performed on the surface of H13 steel using an RH-700 numerical control Nd: YAG solid-state laser. The wavelength of a YAG solid-state laser is 1064 nm, the laser spot diameter range is 2.5–3 mm, and the defocus is 20 mm.

A fully automated Vickers hardness tester was used to study the Vickers hardness (HV) of the coated surface of the samples. Adjust the coating image to be clear and have an appropriate loading height through a 50× optical microscope, select the tested area, and load a diamond-shaped indenter on the surface of the sample with a loading force of 0.2 kg and a loading retention time of 10 s. Measure multiple points in each area and take the average of the results.

The specimens were cut into 10 mm × 10 mm × 5 mm dimensions using an EDM wire cutter. Each specimen was prepared on an automatic polishing machine with 200 #~2000 # silicon carbide sandpaper and polished with diamond polishing liquid. Using aqua regia (a mixture of concentrated nitric acid and concentrated hydrochloric acid in a ratio of 1:3) as an etchant, evenly apply aqua regia to the surface of the sample for approximately 1 min. After etching is completed, the surface of the sample is cleaned and treated to remove residual aqua regia components. After the metallographic specimens were prepared, the microstructure of the cladding layer of specimens was observed using a JEOL JSM-IT200A scanning electron microscope.

The phases of the different high-entropy alloy material systems were characterized using a Rigaku Ultima IV X-ray diffractometer (Tokyo, Japan). The testing conditions are Cu target (λ = 0.1541 nm), Kα radiation, tube voltage of 40 Kv, tube current of 40 mA, scanning range of 20–90°, and the scanning accuracy is improved by slow scanning with a step size of 0.02. The scanned data are imported into Jade software, and the presence of the phase is determined by comparing the diffraction peaks with the diffraction PDF cards of the standard phase.

4. Results and Analysis

4.1. ANOVA for the Effect of Process Parameters on Coating Dilution Rate

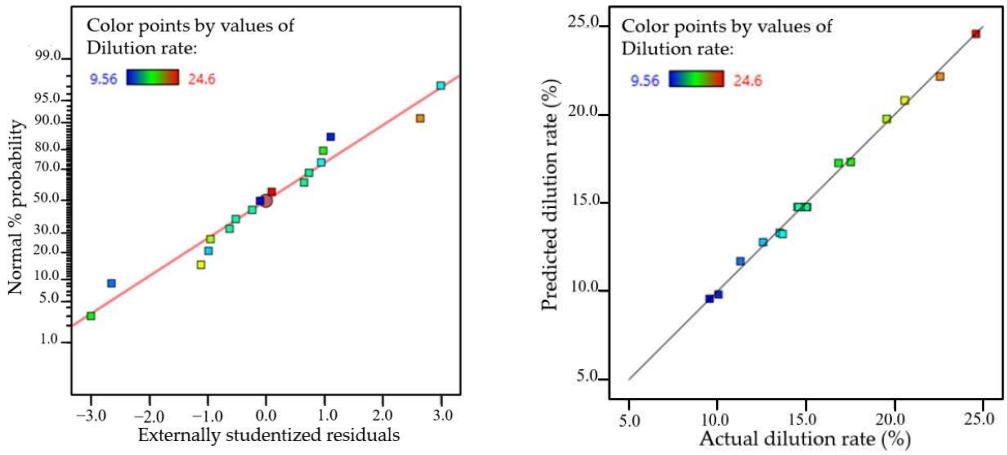
An analysis of variance model was developed for the dilution ratios of different process parameters. The F-value of the model is 177.98 with a *p*-value less than 0.05, indicating that the model is statistically significant. The factors affecting the coating dilution rate were P > V > P^2 > PP_0 > V^2, and the corresponding F-values of each factor were 1311.89 > 208.97 > 54.32 > 14.89 > 6.83, with an R^2 value of 0.9956, which indicated that the model could be used to explain more than 99.56% of the data bias. Taking into account the effect of significant terms on the dilution rate, the regression equation for the dilution rate based on coded and actual values is expressed by Equations (3) and (4).

$$\eta_{code} = 14.77 + 5.36P - 2.14V - 0.8075PP_0 + 1.5P^2 \quad (3)$$

$$\eta_{actual} = -11.77536 + 0.002124 \times P - 2.91072 \times V - 0.004038 \times PP_0 + 0.000038 \times P^2 \quad (4)$$

where η is the dilution rate, %; P is laser power, W; V is cladding speed, mm/s; and P_0 is the pulse width, ms.

Figure 3a shows a normally distributed probability plot of the residuals for the high-entropy alloy coating, which is a graphical representation of the data set compared to a normal distribution. The normally distributed probability plot diagnoses the statistical assumptions of the data analysis and is used in conjunction with the standardized residuals in this regression model to show whether the error term is normally distributed or not [17]. As a result, the points in Figure 3a are approximated as straight lines, which implies that the residuals are normally distributed. This suggests a sufficient link between the model and the experimental data [18]. Figure 3b shows that the predicted dilution response output is consistent with the actual experimental data. Consequently, the dilution rate model has high accuracy.

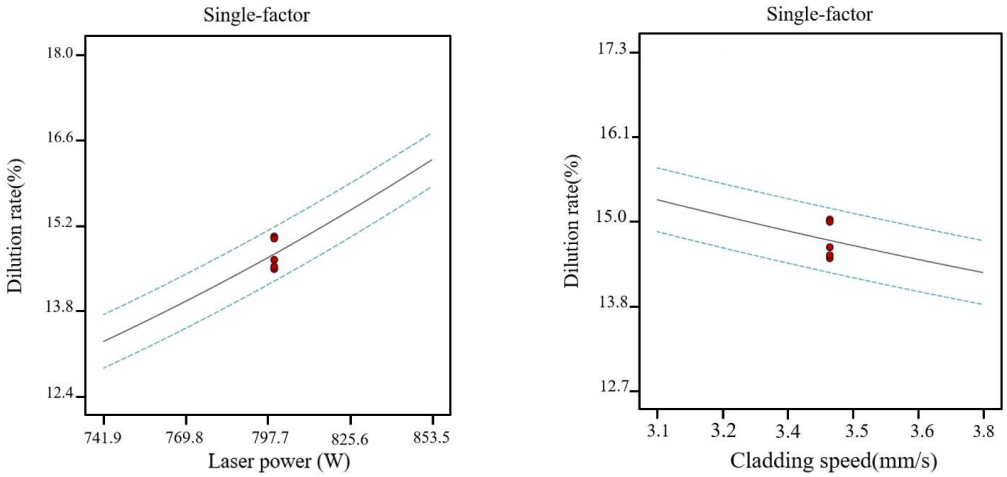


(**a**) (**b**)

Figure 3. Dilution rate: (**a**) probability plot of normal distribution of residuals; (**b**) comparison of predicted and residual values.

4.1.1. Effect of Single Factor on Dilution Rate

Figure 4 shows the variation of the dilution rate under the action of a single factor, from which the effect of a single factor variable on the dilution rate of high-entropy alloy coatings can be seen. Figure 4a,b show the relationship between laser power, cladding speed, and dilution rate, respectively. As the laser power increases, the dilution rate increases, and conversely, the cladding speed increases and the dilution rate continues to decrease. That is, the dilution rate of the coating is positively correlated with the laser power and negatively correlated with the cladding speed. Therefore, decreasing the laser power or increasing the cladding speed can contribute to a reduction in the dilution rate, a result that agrees with Huang et al. [19].



(**a**) (**b**)

Figure 4. Changes in dilution rate for single factor effects: (**a**) changes in dilution rate of laser power effect; (**b**) changes in dilution rate of cladding speed effect.

4.1.2. Effect of Interaction Terms on Dilution Rate

Figure 5 shows the relationship between the interaction term and the dilution rate, illustrating the effect of the interaction of the two factors on the dilution rate of the high-entropy alloy coating. Figure 5a shows the variation plot of the interaction between laser power and pulse width, which appears as two non-parallel lines, indicating that the effect of one factor in the model depends on the other, implying that these factors have a strong influence on the output response [20]. Thus, the interaction between laser power and pulse

width has a significant effect on the dilution rate. Figure 5b,c show the interaction between laser power and cladding speed, as well as pulse width and cladding speed, which are parallel to each other, suggesting that the interaction between the two does not interfere too much with the dilution rate. This is consistent with the experimental data from ANOVA analysis of the dilution rate.

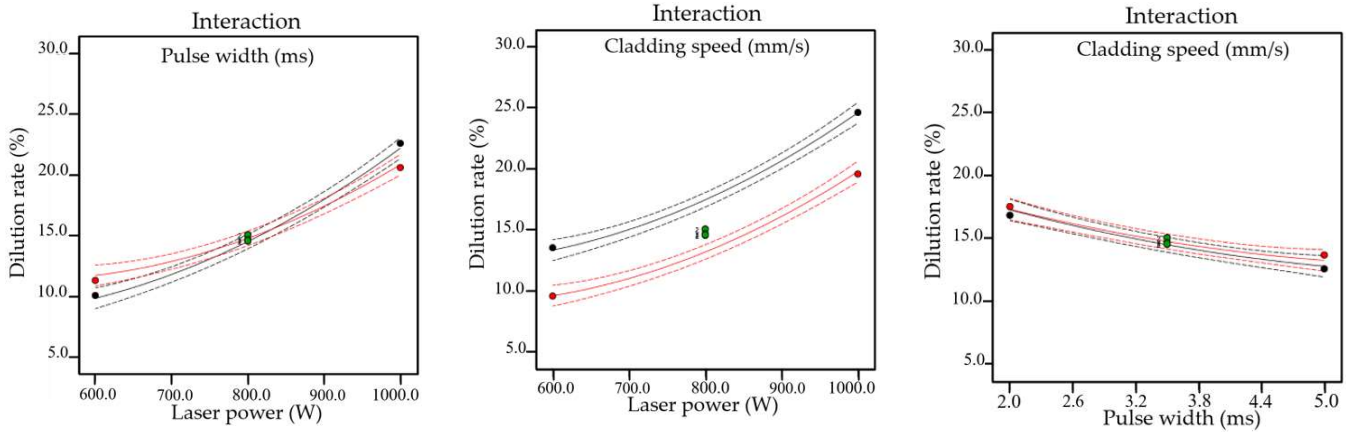


Figure 5. Diagram of the interaction term vs. dilution rate: (**a**) the influence of the interaction between laser power and pulse width on dilution rate; (**b**) the influence of the interaction between laser power and cladding speed on dilution rate; (**c**) the influence of the interaction between pulse width and cladding speed on dilution rate.

4.1.3. Effect of Process Parameters on Dilution Rate

Figure 6 shows a perturbation diagram of the effect of process parameters on the dilution rate. The perturbation diagram typically visualizes how the behavior of a system or model changes when subjected to small deviations or changes (perturbations). The curvature of the perturbation diagram can reflect the sensitivity of process parameters to the output response, and the steeper the slope, the more significant the influence [21]. Figure 6a reveals that the laser power has the largest effect on the dilution rate with a positive correlation, which is consistent with the experimental results in Figure 4a. Specifically, as the laser power increases, the melting capacity of the powder increases, leading to a corresponding increase in the weld pool. The increased melting capacity of the powder yields an increase in the height of the cladding layer, and while more energy is absorbed by the substrate portion, the dilution rate will increase with the rise in the laser power [22]. Similar conclusions were obtained by Erfanmanesh et al. [23] in other studies. The effect of cladding speed on the dilution rate is negatively correlated, which is consistent with the experimental results presented in Figure 4b. Specifically, as the cladding speed increases, the dilution decreases due to the reduced contact of the laser beam with the substrate, which can be attributed to the shading effect of the metal powder. The attenuation rate of laser energy is roughly proportional to the powder supply rate [22]. In addition, the pulse width has little effect on the dilution rate, which is consistent with the experimental data from the ANOVA analysis of the dilution rates. The contour plots in Figure 6b–d illustrate the interactions between laser power and cladding speed, laser power and pulse width, cladding speed and pulse width, as well as cladding speed and pulse width, respectively. Figure 6b shows that decreasing the laser power or increasing the scanning speed contributes to reduce dilution. Figure 6c shows that the dilution rate increases with increasing laser power in the pulse width range. In addition, if the laser power is kept constant, the dilution rate will not change much at higher or lower pulse widths. As shown in Figure 6d, the interaction term between pulse width and cladding speed has no significant effect on the dilution rate, which is consistent with the experimental results in Figure 5.

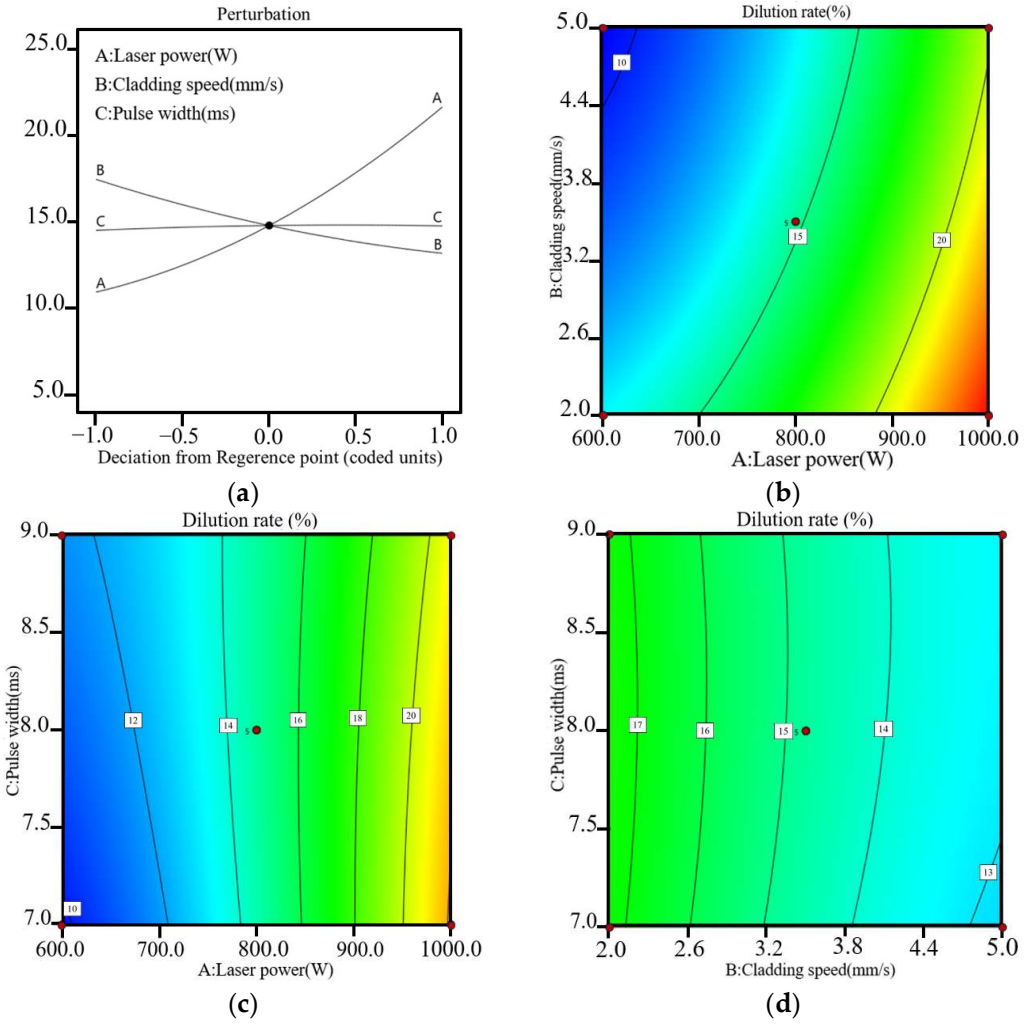


Figure 6. Effect of process parameters on dilution rate: (**a**) perturbation diagram; (**b**) the contour plots of the influence of the interaction between laser power and cladding speed on dilution rate; (**c**) the contour plots of the influence of the interaction between laser power and pulse width on dilution rate; (**d**) the contour plots of the influence of the interaction between cladding speed and pulse width on dilution rate.

4.2. ANOVA Analysis for the Effect of Process Parameters on Coating Microhardness

An analysis of variance model for microhardness with different process parameters was established. The F-value of this model is 8.99 and the *p*-value is less than 0.05, indicating that the model is significant. The factors affecting the microhardness of the coating were $P^2 > P > PP_0 > V > VP_0$, and the corresponding F values of the factor were 24.98 > 22.43 > 10.18 > 7.25 > 5.81. The R^2 value of 0.9204 indicates that the model can be used to explain more than 92.04% of the data bias. Finally, considering the effect of significant terms on microhardness, the microhardness regression equations based on coded and actual values are expressed in Equations (5) and (6).

$$\text{microhardness}_{\text{code}} = 716.87 - 5.69P - 3.23V - 8.27P^2 + 5.42PP_0 + 4.09VP_0 \quad (5)$$

$$\text{microhardness}_{\text{actual}} = 1134.64386 + 0.051035P - 39.61311V - 0.000207P^2 + 2.72833PP_0 + 2.72088VP_0 \quad (6)$$

where P is laser power, W; V is cladding speed, mm/s; and P_0 is the pulse width, ms.

Figure 7 shows the normal distribution probability plot of the microhardness residuals compared with the predicted and actual values. The normal distribution probability plots in Figure 7a,b are approximately linear with the predicted and actual values, indicating

that the residuals are normally distributed, i.e., there is a strong correlation between the microhardness model and the experimental data. As a result, the microhardness model has a high degree of accuracy.

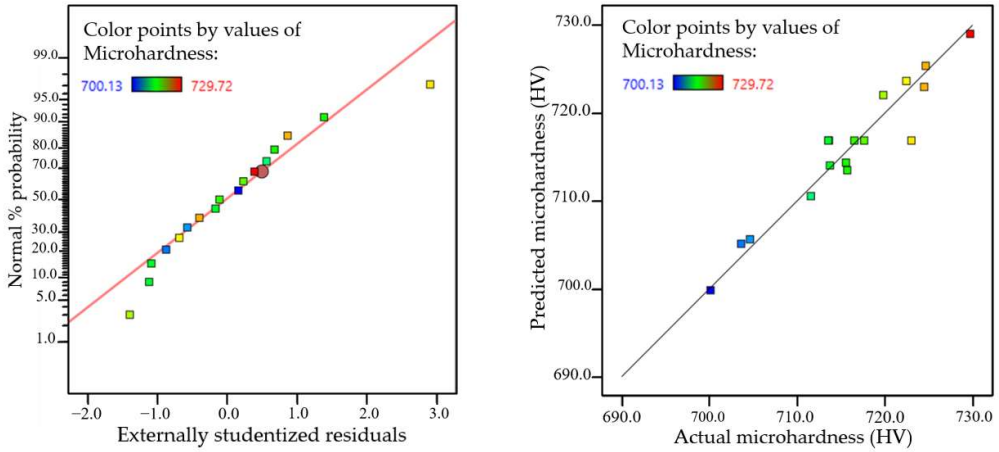


Figure 7. Microhardness: (**a**) probability plot of normal distribution of residuals; (**b**) comparison of predicted and actual values.

4.2.1. Effect of Single Factor on Microhardness

Figure 8a,b show the relationship between laser power, cladding speed, and microhardness, respectively. As the laser power increases, the microhardness first increases and then decreases. Meanwhile, the microhardness decreases slowly with the increase in cladding speed, which indicates that the microhardness characteristics can be improved by the appropriate laser power and cladding speed.

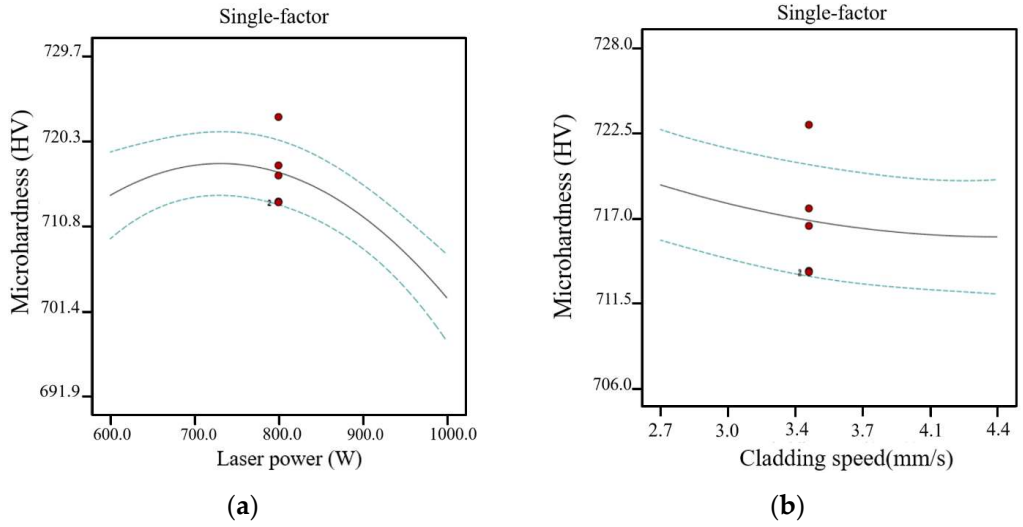
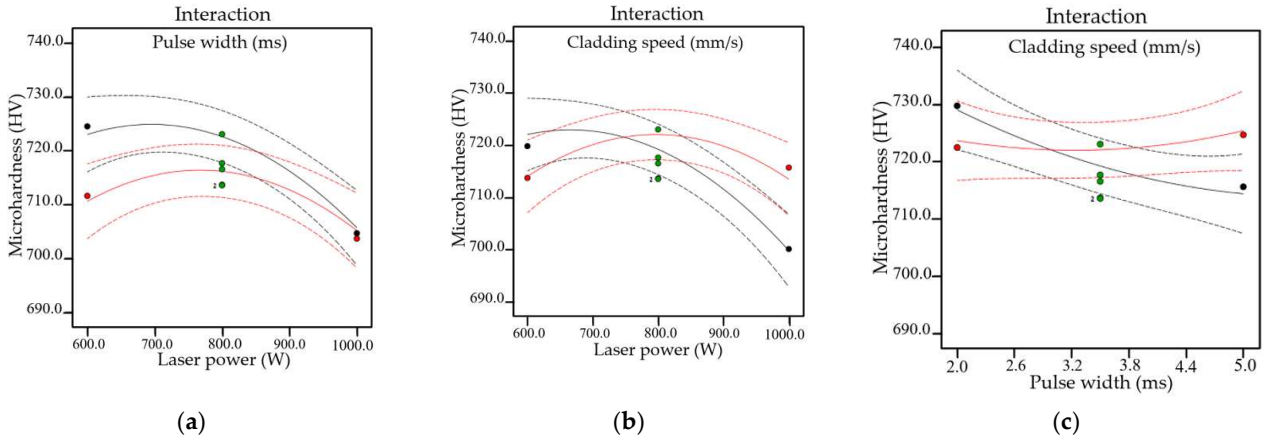


Figure 8. Changes in microhardness for single factor effects: (**a**) changes in microhardness of laser power effect; (**b**) changes in microhardness of cladding speed effect.

4.2.2. Effect of Interaction Terms on Microhardness

Figure 9 shows the relationship between the different interaction terms and the microhardness. The two factors in Figure 9b,c are presented as two non-parallel lines, indicating that the interaction between laser power and cladding speed as well as pulse width and cladding speed has a significant coupling effect on the microhardness of the high-entropy alloy coating, whereas the interaction between laser power and pulse width has a less significant effect on the microhardness.



(**a**) (**b**) (**c**)

Figure 9. Diagram of the interaction term vs. microhardness: (**a**) the influence of the interaction between laser power and pulse width on microhardness; (**b**) the influence of the interaction between laser power and cladding speed on microhardness; (**c**) the influence of the interaction between pulse width and cladding speed on microhardness.

4.2.3. Effect of Process Parameters on Microhardness

Figure 10 shows the perturbation plot of the microhardness for different process parameters. The microhardness of the coating increases and then decreases with the increment in laser power [24]. Dada et al. also published a similar view that the hardness value of AlTiCrFeCoNi HEA decreases with increasing laser power [25]. Also, the increase in cladding speed has a negative effect on the microhardness of the coating. Compared with the melting speed, the influence of laser power on the curvature of the hardness curve is relatively small, and the sensitivity of changes in hardness values to laser power is greater than that of cladding speed [26].

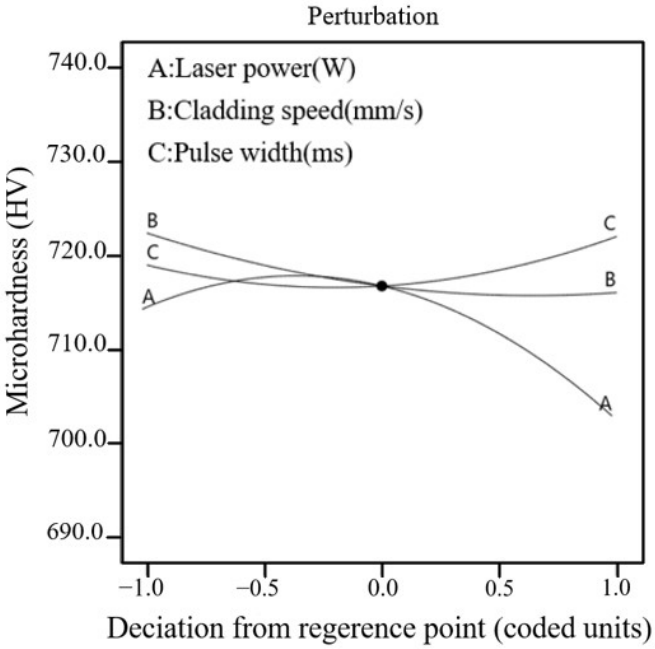


Figure 10. Effect of process parameters on microhardness: perturbation diagram.

According to the disturbance diagram and Table 2, when the melting speed is constant, the high hardness HEA coating is mainly concentrated at a laser power of 600 W–800 W. When the laser power is 600 W and the cladding speed is 5 mm/s, the microhardness of the coating is relatively low, at 711.56 HV. This is because when the laser power is low, the energy of the generated beam is also low, reducing the energy density, resulting in

less energy absorption by HEA powder, which solidifies in the coating without forming a molten state. These powders solidify in the coating without forming a molten state, which cannot fully produce the effect of solid solution strengthening, ultimately leading to a decrease in its hardness [27]. In addition, when the laser power reaches 1000 W and the cladding speed is 2 mm/s, the hardness also decreases to 704.62 HV. This is because the laser beam stays on the substrate for too long, and too much energy is absorbed by the HEA powder, causing a small amount of powder to burn. This powder cannot enhance the coating performance, resulting in a decrease in the microhardness of the HEA coating [27]. In contrast, the pulse width has little effect on the microhardness, as shown by its smaller F- and *p*-values. The combination of the perturbation plots in Figures 6 and 10 show that laser power and cladding speed have opposite effects on dilution and microhardness, i.e., GAO [28] et al. also reached similar conclusions. There is an inverse ratio between microhardness and the dilution rate, so that the dilution rate of the coatings decreases with an increase in microhardness.

4.3. Optimization and Characterization

According to the prediction model, the optimal process parameters were laser power P = 676.73 W, cladding speed V = 5 mm/s, and pulse width P_0 = 9 ms. A high-entropy alloy coating, CoCrFeNiTiAl, was prepared using the optimized process parameters. The performance of the high-entropy alloy coating was evaluated based on the optimization process parameters determined through response surface methodology.

Figure 11 shows the macroscopic cross-section and macroscopic surface of the CoCrFeNiTiAl high-entropy alloy coating, respectively. The macroscopic cross-sectional morphology of the coating is shown in Figure 11a. It can be seen that the specimen consists of the cladding layer and a matrix. A metallurgical bond has formed between the coating and the substrate, indicated by the yellow dashed line marking the cladding interface. Figure 11b shows the macroscopic surface of the coating.

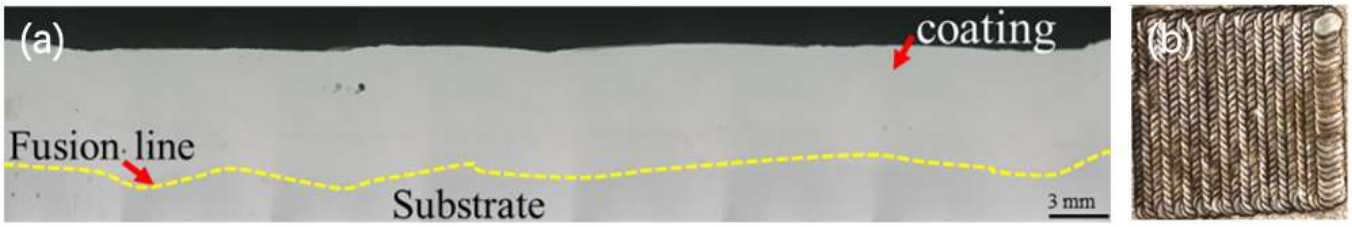


Figure 11. (**a**) Macroscopic cross-section of the coating; (**b**) macroscopic surface of the coating.

Figure 12 shows the XRD pattern of CoCrFeNiTiAl high-entropy alloy coatings. The analysis of the diffraction peaks showed that characteristic peaks of the FCC lattice (face-centered cube), BCC lattice (body-centered cube), and ordered BCC (B2) were present. Among them, the BCC structure (B2) was identified as an AlNi compound through known peaks in the ICDD/JCPDS card (PDF—# 20-0019). Previous studies have shown that [29] the appearance of the BCC structure or FCC structure is related to the valence electron concentration (VEC). It was concluded that the FCC phases are stable at a higher VEC ($\geq$8), while the BCC phases are stable at a lower VEC ($\leq$6.87). When the VEC is between 6.87 and 8.0, both FCC and BCC phases can exist. The VEC is defined in Equation (7).

$$\mathrm{VEC} = \sum_{i=1}^{n} C_i (\mathrm{VEC})_i \tag{7}$$

where $(\mathrm{VEC})_i$ is the VEC of the i-th component. In this study, the VEC of the AlCoCrFeNiTi HEA coating is 7.72. The XRD analysis is confirmed by the above prediction criteria.

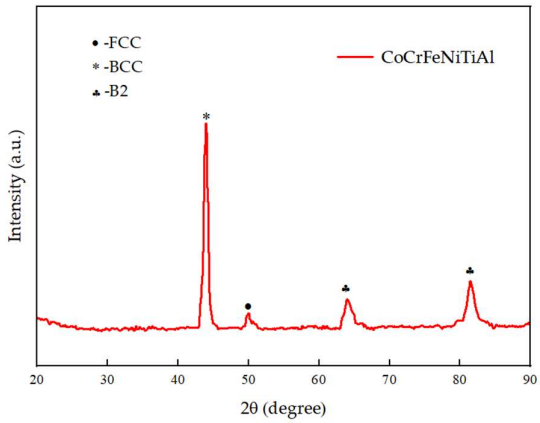
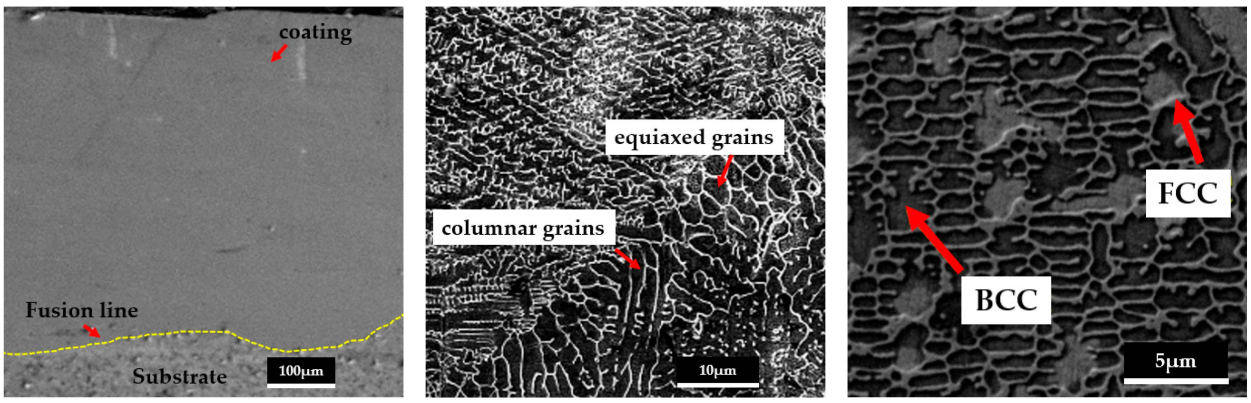


Figure 12. Phase XRD pattern of CoCrFeNiTiAl high-entropy alloy coating.

The diffraction peak of the BCC phase is stronger, while the diffraction peak intensity of the FCC phase shows the opposite characteristics. Compared with the FCC structure, the BCC structure has a compact packing surface of {110}, and each slip surface has one less slip direction than the face-centered cube, making it more difficult to slip. Therefore, higher stress is required to propagate slip. Moreover, at the atomic scale, the {110} surface density is smaller and more irregular, the atomic arrangement is tighter, and the interaction force between atoms is stronger, making the material more difficult to deform, resulting in BCC structures having a higher hardness than FCC structures [30]. This suggests that the formation of a BCC structure is the main hardening factor because the larger the volume fraction of the BCC phase, the higher the hardness value exhibited by the alloy coating [31]. The CoCrFeNiTiAl high-entropy alloy coating prepared by optimal process parameters has high hardness values.

Figure 13 shows the SEM images of the cross-sectional microstructure of the junction between the cladding layer and the matrix of the CoCrFeNiTiAl high-entropy alloy prepared using the optimized process parameters, which displays the microstructure characteristics of the material at different magnifications. Figure 13a shows that the metallurgical bond formed between the cladding layer and the matrix is strong, and there are no obvious defects such as pores and cracks. Figure 13b shows that the microstructure of the high-entropy alloy coating is mainly equiaxed crystallite, and the equiaxed crystallites are closely arranged. The columnar crystallites perpendicular to the cladding interface are also observed, showing the coexistence of equiaxed grains and columnar grains with well-defined grain and crystallite boundaries. Figure 13c clearly shows the FCC structure and BCC structure, and similar results were observed in the XRD spectrum.



(**a**) (**b**) (**c**)

Figure 13. SEM images: (**a**) the cross-sectional microstructure of the cladding-matrix junction; (**b**) 10× magnification of Figure (**a**); (**c**) 20× magnification of Figure (**a**).

To investigate the influence of coating microstructure on performance, the crystallite size D was calculated using the Scherrer equation [32], as in Equation (8).

$$D = \frac{k\lambda}{\beta\cos\theta} \tag{8}$$

where D is the average crystallite size, nm; k is the Scherrer constant of 0.89; λ is 0.154056, nm; θ is the diffraction angle position of the XRD peak, rad; and β is the full width at the half maximum (FWHM) of the peak at θ (rad). The crystallite size of the coating is 179.32 nm. Compared with CoCrFeNiTiAl high-entropy alloy powder that has not undergone laser cladding, the CoCrFeNiTiAl high-entropy alloy coating has a fine crystallite structure and smaller crystallite size. The smaller the crystallite size, the higher the material hardness, which increases the solubility, produces a lattice distortion effect and a solid solution effect, and improves the hardness and corrosion resistance of the coating [33].

The microstructure of the CoCrFeNiTiAl high-entropy alloy coating prepared by optimal parameters is dominated by equiaxial and columnar grains, and the phase is an FCC + BCC + B2 composite structure with fine structural grains, which improves the hardness and corrosion resistance of the coating. The test results of XRD and SEM verify that it is feasible to optimize the process parameters for the preparation of high-performance high-entropy alloys by the response surface optimization method.

5. Conclusions

In order to optimize the best process parameters for the preparation of high-performance high-entropy alloy coatings, the influence of process parameters on the output response was systematically investigated based on the response surface method, and the following conclusions were drawn.

(1) Among the single factors, the laser power has the greatest effect on the properties of high-entropy alloy coatings, followed by the cladding speed, and pulse width has no significant effect. Notably, the dilution rate of the coating is positively correlated with the laser power and negatively with the cladding speed. The microhardness shows a tendency of increasing and then decreasing with the increase in laser power, and the microhardness decreases slowly with the increase in cladding speed.

(2) In the interaction term analysis, the interaction term of laser power and pulse width has significant effects on the evaluation of the two output responses, while the interaction term of pulse width and cladding speed has a significant effect only on microhardness, while the interaction term of laser power and cladding speed has no significant effect on the evaluation of the two output responses.

(3) According to the model prediction, the optimal parameters for laser melting and cladding of CoCrFeNiTiAl high-entropy alloy coatings are the laser power P = 676.73 W, cladding speed V = 5 mm/s, and pulse width P_0 = 9 ms.

(4) The microstructure of the CoCrFeNiTiAl high-entropy alloy coating prepared by optimal parameters is dominated by equiaxial and columnar grains, and the phase is an FCC + BCC + B2 composite structure with fine structural grains, which improves the hardness and corrosion resistance of the coating.

Author Contributions: Conceptualization, B.J. and Y.Z.; methodology, C.L. and Y.Z.; validation, Y.Z. and F.S.; formal analysis, Z.H., C.L. and H.L.; investigation, C.L., H.W. and H.L; resources, B.J., H.W. and F.S.; data curation, Z.H. and C.L.; writing—original draft preparation, B.J., Z.H. and C.L.; writing—review and editing, B.J., Y.Z. and F.S.; visualization, C.L. and H.L.; supervision, Y.Z.; project administration, Z.H. and C.L.; funding acquisition, B.J. All authors have read and agreed to the published version of the manuscript.

Funding: This research was funded by the Dongguan Key Laboratory of Surface Technology and Functional Materials Preparation, Grant No. 20231600400352) and the APC was funded by B.J.

Data Availability Statement: Data are contained within the article.

Conflicts of Interest: The authors declare no conflicts of interest.

References

1. Li, W.D.; Xie, D.; Li, D.Y.; Zhang, Y.; Gao, Y.F.; Liaw, P.K. Mechanical behavior of high-entropy alloys. *Prog. Mater. Sci.* **2021**, *118*, 100777. [CrossRef]
2. George, E.P.; Raabe, D.; Ritchie, R.O. High-entropy alloys. *Nat. Rev. Mater.* **2019**, *4*, 515–534. [CrossRef]
3. Rao, Z.; Tung, P.Y.; Xie, R.W.; Wei, Y.; Zhang, H.B.; Ferraei, A.; Klaver, T.P.C.; Sukumar, P.T.; Raabe, D. Machine learning–enabled high-entropy alloy discovery. *Science* **2022**, *378*, 78–85. [CrossRef] [PubMed]
4. Ye, Y.F.; Wang, Q.; Lu, J.; Liu, C.T.; Yang, Y. High-entropy alloy: Challenges and prospects. *Mater. Today* **2016**, *19*, 349–362. [CrossRef]
5. Tokarewicz, M.; Grądzka-Dahlke, M. Review of recent research on AlCoCrFeNi high-entropy alloy. *Metals* **2021**, *11*, 1302. [CrossRef]
6. Ji, W.; Fu, Z.Y.; Wang, W.M.; Wang, H.; Zhang, J.Y.; Wang, Y.C.; Zhang, F. Mechanical alloying synthesis and spark plasma sintering consolidation of CoCrFeNiAl high-entropy alloy. *J. Alloys Compd.* **2014**, *589*, 61–66. [CrossRef]
7. Joseph, J.; Haghdadi, N.; Shamlaye, K.; Hodgson, P.; Barnett, M.; Fabijanic, D. The sliding wear behaviour of CoCrFeMnNi and AlxCoCrFeNi high entropy alloys at elevated temperatures. *Wear* **2019**, *428*, 32–44. [CrossRef]
8. Xiong, W.; Guo, A.X.Y.; Zhan, S.; Liu, C.T.; Cao, S.C. Refractory high-entropy alloys: A focused review of preparation methods and properties. *J. Mater. Sci. Technol.* **2023**, *142*, 196–215. [CrossRef]
9. Lu, K.F.; Zhu, J.; Ge, W.Q.; Hui, X.D. Progress on new preparation methods, microstructures, and protective properties of high-entropy alloy coatings. *Coatings* **2022**, *12*, 1472. [CrossRef]
10. Zhu, L.D.; Xue, P.S.; Lan, Q.; Meng, G.R.; Ren, Y.; Yang, Z.C.; Xu, P.H.; Liu, Z. Recent research and development status of laser cladding: A review. *Opt. Laser Technol.* **2021**, *138*, 106915. [CrossRef]
11. DebRoy, T.; Wei, H.L.; Zuback, J.S.; Mukherjee, T.; Elmer, J.W.; Milewski, J.O.; Beese, A.M.; Wilson-Heid, A.; De, A.; Zhang, W. Additive manufacturing of metallic components–process, structure and properties. *Prog. Mater. Sci.* **2018**, *92*, 112–224. [CrossRef]
12. Zhang, Y.; Bai, P.K.; Li, Z.H.; Zhang, J.; Liu, W.J. Multi-objective optimization of laser cladding process parameters for Q345B steel. *Mater. Today Commun.* **2024**, *39*, 108679. [CrossRef]
13. Xu, H.Y.; Lu, J.B.; Peng, X.; Ma, M.X. Microstructure and Properties of Laser Cladding CoCrCu0.4FeNi High Entropy Alloy Coating. *Surf. Technol.* **2023**, *52*, 418–428.
14. Shu, F.Y.; Zhang, B.L.; Liu, T.; Sui, S.H.; Liu, Y.X.; He, P.; Liu, B.; Xu, B.S. Effects of laser power on microstructure and properties of laser cladded CoCrBFeNiSi high-entropy alloy amorphous coatings. *Surf. Coat. Technol.* **2019**, *358*, 667–675. [CrossRef]
15. Cao, Q.; Lian, G.F.; Chen, C.R.; Feng, M.Y. Sensitivity analysis of the process parameters of laser cladding NiCrCoAlY. *Metall. Res. Technol.* **2022**, *119*, 206. [CrossRef]
16. Durakovic, B. Design of experiments application, concepts, examples: State of the art. *Period. Eng. Nat. Sci.* **2017**, *5*, 421–439. [CrossRef]
17. Olorundaisi, E.; Jamiru, T.; Adegbola, T.A.; Ogunbiyi, O.F. Modeling and optimization of operating parameters using RSM for mechanical behaviour of dual phase steels. *Mater. Res. Express* **2019**, *6*, 105628. [CrossRef]
18. Danmaliki, G.I.; Saleh, T.A.; Shamsuddeen, A.A. Response surface methodology optimization of adsorptive desulfurization on nickel/activated carbon. *Chem. Eng. J.* **2017**, *313*, 993–1003. [CrossRef]
19. Huang, Y.B.; Hu, Y.L.; Zhang, M.J.; Mao, C.; Wang, K.M.; Tong, Y.G.; Zhang, J.; Li, K.W. Multi-objective optimization of process parameters in laser cladding CoCrCuFeNi high-entropy alloy coating. *J. Therm. Spray Technol.* **2022**, *31*, 1985–2000. [CrossRef]
20. Sundararaman, K.A.; Padmanaban, K.P.; Sabareeswaran, M. Optimization of machining fixture layout using integrated response surface methodology and evolutionary techniques. *Proc. Inst. Mech. Eng. Part C J. Mech. Eng. Sci.* **2016**, *230*, 2245–2259. [CrossRef]
21. Yu, D.W.; Qing, X.T.; Lin, H.Y.; Yang, J.; Yang, J.C.; Wang, X.J. Response Surface Methodology Optimization of Resistance Welding Process for Unidirectional Carbon Fiber/PPS Composites. *Materials* **2024**, *17*, 2176. [CrossRef] [PubMed]
22. Saeedi, R.; Razavi, R.S.; Bakhshi, S.R.; Erfanmanesh, M.; Bani, A.A. Optimization and characterization of laser cladding of NiCr and NiCr–TiC composite coatings on AISI 420 stainless steel. *Ceram. Int.* **2021**, *47*, 4097–4110. [CrossRef]
23. Erfanmanesh, M.; Abdollah-Pour, H.; Mohammadian-Semnani, H.; Shoja-Razavi, R. An empirical-statistical model for laser cladding of WC-12Co powder on AISI 321 stainless steel. *Opt. Laser Technol.* **2017**, *97*, 180–186. [CrossRef]
24. Chen, L.Y.; Yu, T.B.; Chen, X.; Zhao, Y.; Guan, C. Process optimization, microstructure and microhardness of coaxial laser cladding TiC reinforced Ni-based composite coatings. *Opt. Laser Technol.* **2022**, *152*, 108129. [CrossRef]
25. Dada, M.; Popoola, P.; Mathe, N.; Pityana, S.; Adeosun, S. Parametric optimization of laser deposited high entropy alloys using response surface methodology (RSM). *Int. J. Adv. Manuf. Technol.* **2020**, *109*, 2719–2732. [CrossRef]
26. Pan, L.K.; Wang, C.C.; Hsiao, Y.C.; Ho, K.C. Optimization of Nd: YAG laser welding onto magnesium alloy via Taguchi analysis. *Opt. Laser Technol.* **2005**, *37*, 33–42. [CrossRef]
27. Ren, X.Y.; Sun, W.L.; Gao, L.S.; Tian, S.; Lin, H.B. Multi-response multi-parameter optimization of CoCrFeNiMo0.2 HEA coatings prepared by internal laser cladding and tribological behaviors. *Mater. Today Commun.* **2024**, *40*, 109643. [CrossRef]
28. Gao, S.A.; Fu, Q.; Li, M.Z.; Huang, L.; Liu, N.; Cui, C.; Yang, B.; Zhang, G.D. Optimization of Laser Cladding Parameters for High-Entropy Alloy-Reinforced 316L Stainless-Steel via Grey Relational Analysis. *Coatings* **2024**, *14*, 1103. [CrossRef]
29. Liu, H.; Liu, J.; Chen, P.J.; Yang, H.F.; Hao, J.B.; Tian, X.H. Microstructure and properties of AlCoCrFeNiTi high-entropy alloy coating on AISI1045 steel fabricated by laser cladding. *J. Mater. Eng. Perform.* **2019**, *28*, 1544–1552. [CrossRef]
30. Reed-Hill, R.E.; Abbaschian, R.; Abbaschian, R. *Physical Metallurgy Principles*; Van Nostrand: New York, NY, USA, 1973.

31. Wang, W.R.; Wang, W.L.; Wang, S.C.; Tsai, Y.C.; Lai, C.H.; Yeh, J.W. Effects of Al addition on the microstructure and mechanical property of AlxCoCrFeNi high-entropy alloys. *Intermetallics* **2012**, *26*, 44–51. [CrossRef]
32. Muniz, F.T.L.; Miranda, M.A.R.; Morilla dos Santos, C.; Sasaki, J.M. The Scherrer equation and the dynamical theory of X-ray diffraction. *Acta Crystallogr. Sect. A Found. Adv.* **2016**, *72*, 385–390. [CrossRef] [PubMed]
33. Xu, Y.K.; Li, Z.Y.; Liu, J.R.; Chen, Y.N.; Zhang, F.Y.; Wu, L.; Hao, J.M.; Liu, L. Microstructure evolution and properties of laser cladding CoCrFeNiTiAl x high-entropy alloy coatings. *Coatings* **2020**, *10*, 373. [CrossRef]

Disclaimer/Publisher's Note: The statements, opinions and data contained in all publications are solely those of the individual author(s) and contributor(s) and not of MDPI and/or the editor(s). MDPI and/or the editor(s) disclaim responsibility for any injury to people or property resulting from any ideas, methods, instructions or products referred to in the content.